INSPYRE
Investigations Supporting MOX Fuel Licensing in ESNII Prototype Reactors

EERA JPNM
JOINT PROGRAMME ON NUCLEAR MATERIALS

D6.1 – Review of available models and progress on the sub-models dealing with the intra- and intergranular inert gas behaviour

D. Pizzocri, L. Luzzi, T. Barani, L. Cognini, A. Magni (Polimi),
A. Schubert, P. Van Uffelen, T. Wiss (JRC)

Version 1 – 05/02/2019

The INSPYRE project has received funding from the EURATOM research and training programme 2014-2018 under Grant Agreement No 754329.

Document type	Deliverable
Document number	D6.1 version 1
Document title	Review of available models and progress on the sub-models dealing with the intra- and intergranular inert gas behaviour
Authors	D. Pizzocri, L. Luzzi, T. Barani, L. Cognini, A. Magni (Polimi), A. Schubert, P. Van Uffelen, T. Wiss (JRC)
Release date	05/02/2019
Contributing partners	Polimi, JRC
Dissemination level	Public

Version	Short description	Main author	WP leader	Coordinator
1	First release	D. Pizzocri (Polimi) 02/01/2019	A. Del Nevo (ENEA) 04/02/2019	M. Bertolus (CEA) 05/02/2019

SUMMARY

Current modelling of inert gas behaviour (IGB) in fuel performance codes (FPCs) is mainly correlation-based and tailored to light water reactors conditions and for uranium dioxide. Task 6.1 of INSPYRE aims at overcoming these limitations by developing physics-based mesoscale IGB models allowing fuel performance codes to effectively simulate the IGB in mixed oxide fuels in fast reactor conditions. Physics-based models are developed to progressively replace purely empirical correlations. These models allow the implementation of a multiscale approach, in which model parameters derived from lower length scale calculations or measurements (arising from other WPs and open literature) are used by mesoscale models. Final step in the multiscale approach is the inclusion of mesoscale models in FPCs, which is the target of Task 7.1 of INSPYRE.

In this deliverable, we present the progress achieved towards IGB modelling for FR MOX during the first year of the INSPYRE project. The models considered are either developed specifically for MOX fuels or are developed for other fuel materials but extendable to MOX fuels. Models are categorized among those describing intra-granular and inter-granular IGB, as well as the particular IGB in the high burn-up structure and in restructured grains. The inert gases considered are xenon, krypton and helium, the last one playing a significant role in MOX fuels compared to UO_2. We then present the progress made with respect to state-of-the-art models available in FPCs. The focus is on helium production, diffusivity and solubility; on the modelling approach used to describe the formation of high burn-up structure and on the modelling approach adopted for the treatment of diffusion in restructured grains. Finally, we outline the future model developments envisaged and we clarify the verification and validation strategy, as well as the uncertainty and sensitivity analyses, planned to assess the developed models prior to their integration in fuel performance codes.

CONTENT

GLOSSARY

BWR	Boiling Water Reactor
EBSD	Electron Backscatter Diffusion
FGR	Fission Gas Release
FPC	Fuel Performance Code
FR	Fast Reactor
FVM	Finite Volume Method
Gen IV	Generation IV
HBS	High Burn-up Structure
IGB	Inert Gas Behaviour
INSPYRE	Investigations Supporting MOX Fuel Licensing for ESNII Prototype Reactors
JPNM	Joint Programme on Nuclear Materials
LAR	Least Absolute Residuals
LFR	Lead-cooled Fast Reactor
LWR	Light Water Reactor
MD	Molecular Dynamics
MOX	Mixed Oxide Fuel
ODE	Ordinary Differential Equation
POD	Proper Orthogonal Decomposition
PDE	Partial Differential Equation
PWR	Pressurized Water Reactor
ROM	Reduced Order Model
SEM	Scansion Electron Microscopy
SFR	Sodium-cooled Fast Reactor
TEM	Transmission Electron Microscopy
WP	Work Package

1 FOREWORD

The current description of inert gas behaviour (IGB) in fuel performance codes (FPCs) presents significant limitations when it comes to mixed oxide (MOX) fuels in fast reactor (FR) conditions [1]–[4]. Three main reasons can be appointed for these limitations

- A limited amount of experimental data concerning IGB is available (in particular compared to UO_2 in light water reactors, LWRs, or even to MOX in LWRs). Limited information is available about the micro- and mesoscale details of inert gas behaviour evolution (in terms of SEM/TEM images).
- High fission gas release (≈ 80%) has been reported for sodium-cooled FRs [5]. These high values of release suggested that detailed description of IGB was not required in FPCs, since conservative assumption such as FGR = 100% were satisfactory from an engineering point of view.
- Several inter-related phenomena connected to IGB occur in FR MOX, e.g., pore migration towards the centre of the pellet, formation of columnar grains, redistribution of uranium and plutonium [6]–[8]. These, paired with the heterogeneous distribution of plutonium agglomerates within the pellet, impose *completely* different treatment with respect to IGB in UO_2, with therefore only limited possibilities of transferring over modelling approaches.

It is fundamental to point out that proper modelling of IGB in FR MOX is fundamental in FPC and that simplified conservative approaches are not enough. Even from a purely engineering point of view, there are indications that expected fission gas release are well below 100% in several designs of Gen-IV FRs (e.g., MYRRHA, ALFRED) [9]–[12]. Moreover, the relative scarcity of experimental data/information calls out for the development of physics-based models instead of correlation-based models. These models can be informed from lower-length scale knowledge (either simulations or experiments) whereas the development of correlations relies on (expensive) integral irradiation experiments. Lastly, physics-based models allow for effective multiscale bridging, gaining better understanding about the detailed mechanisms involved and transferring knowledge acquired from separate effect experiments and lower-length scale calculations to the engineering-scale of FPCs (as demonstrated for UO_2 in LWRs, e.g., [13], [14]). This implies a more efficient and effective use of coordinated research efforts, potentially speeding up the development and licensing of FR MOX.

In this deliverable, we present the progress achieved towards IGB modelling for FR MOX during the first year of the INSPYRE project. Three specific aspects are addressed: (1) intra-granular helium behaviour, for which we detail the governing model equations together with the fundamental parameters (i.e., a meta-model for the helium production rate, new correlations for helium diffusivity and solubility); (2) diffusion of inert gas in columnar grains, for which we present a reduced order model designed and developed for future inclusion in FPCs; and (3) a model describing the formation of HBS and its characteristic depletion of intra-granular gas.

For each of the presented models, we introduce (if any) the current state-of-the-art description available in FPCs (focused but not restricted to TRANSURANUS [15]), and we clarify the status of assessment in terms of verification and validation. In the last section, the main strengths of the presented modelling approaches are summarized, and a clear path forward for their development is provided.

2 PROGRESS TOWARDS INERT GAS BEHAVIOUR MODELLING FOR MOX FUELS IN FAST REACTOR CONDITIONS

2.1 Inert gas behaviour: intra-granular helium

Helium behaviour is of crucial importance in MOX fuel, both in-reactor as well as during storage. Due to the enrichment in plutonium, higher concentrations of minor actinides are produced during irradiation compared to UO_2. A majority of these isotopes undergo α-decay, which are effectively helium nuclei created in the fuel matrix. Secondary mechanisms of helium formation are from ternary fissions (yield around 0.2%) and (n,α)-reactions on ^{16}O for high-energy neutrons.

To describe the intra-granular behaviour of helium in MOX fuel, we propose a model which extends the one proposed by Talip *et al.* [16]. Namely

$$\frac{\partial}{\partial t}c_{\mathrm{He}} = \mathrm{D}_{\mathrm{He}}\frac{1}{r^2}\frac{\partial}{\partial r}r^2\frac{\partial}{\partial r}c_{\mathrm{He}} - \beta\left(c_{\mathrm{He}} - c_{S,\mathrm{He}}\right) + \alpha m_{\mathrm{He}} + \mathrm{S}_{\mathrm{He}} \quad (1)$$

$$\frac{\partial}{\partial t}m_{\mathrm{He}} = \beta\left(c_{\mathrm{He}} - c_{S,\mathrm{He}}\right) - \alpha m_{\mathrm{He}} \quad (2)$$

where c_{He} (at m^{-3}) and m_{He} (at m^{-3}) are the concentration of helium dissolved in the fuel matrix and trapped in intra-granular bubbles, respectively. D_{He} (m^2 s^{-1}) is the diffusion coefficient, β (s^{-1}) is the trapping rate [17], α (s^{-1}) is the re-solution rate [18], [19], and S_{He} (at m^{-3} s^{-1}) is the production rate of helium. $c_{S,\mathrm{He}}$ (at m^{-3}) is the solubility limit of helium in the fuel matrix. t (s) and r (m) are respectively time and the radial coordinate within the fuel grain, assumed as spherical [20]. Eq. 1,2 are to be solved imposing a Dirichlet boundary condition at the grain radius.

Eqs. 1,2 physically describe the behaviour of intra-granular helium. The helium atoms are produced in the fuel matrix. The excess of atoms with respect to the solubility is progressively either trapped into intra-granular bubbles. The trapping process is counteracted by the re-solution of atoms from the intra-granular bubbles caused by the interaction of the fission fragments. The proposed model is thus physics-based and describes helium behaviour at the scale of fuel grains, therefore being in line with the development guidelines detailed in Section 1.

The effective application of Eqs. 1,2 requires the definition of the model parameters specific to helium, i.e., the production rate S_{He}, the diffusion coefficient D_{He}, and the solubility limit $c_{S,\mathrm{He}}$. The first objective of the development of this model is the derivation of these parameters for UO_2. This allows establishing a multiscale methodology readily applicable to MOX fuel as lower-length scale information becomes available within the INSPYRE project.

The next step in the development of this model, in addition to the determination of the parameters described in the following subsections, is its implementation in SCIANTIX [21] and its validation against separate effect data of annealed fuel samples [16], [22]. Then, as new data become available for MOX fuel, the validation will need to be extended.

Production rate S_{He}. In order to calculate the production rate S_{He} it is required to follow the evolution of minor actinides. These isotopes undergo α-decay, essentially producing helium nuclei within the fuel lattice. Dedicated depletion codes allow for tracking the evolution of all the isotopes in the fuel along the irradiation, e.g., Monte Carlo neutronic codes such as SERPENT [23]. The computational requirements of depletion codes are hence hardly affordable in the frame of a fuel performance simulation.

Depletion calculations require access to full microscopic cross section libraries, with cross sections as function of energy (and angle). Macroscopic cross sections are calculated by the depletion code itself considering also the fuel rod composition (which affects the energy spectrum of the neutrons). Nonetheless a depletion calculation embedded in a FPC logically focuses on the nuclides relevant for heat generation by fission – finally determining the relative radial power profile.

Despite of the thus justified simplified approach, a FPC must use macroscopic cross sections that are at least specific to the reactor type (e.g., BWR, PWR, SFR, LFR). Beyond this step, different sets of effective macroscopic cross sections have been implemented if needed - depending on their sensitivity on burn-up and initial enrichment/composition of the fuel. Up to now, there is no standard methodology for generating such datasets, and various neutronic codes (e.g., SCALE, MONTEBURNUS, SERPENT) have been applied for this purpose. For example, in the TUBRNP model (part of the TRANSURANUS fuel performance code) the effective cross sections for neutron-induced fission and capture in UO_2 depend on the reactor type and the initial enrichment of ^{235}U while the related cross sections for LWR-MOX fuel depend on the initial Pu concentration. The absorption of resonance neutrons in ^{238}U and ^{240}Pu is considered implicitly via a radial form factor [24]–[26]. In addition, the dependence of the ^{240}Pu neutron capture cross section on burn-up is accounted for. Important first steps to include the production of Helium in TUBRNP were taken by Botazzoli at el. [27]. While the model was recently also extended to Th-based LWR fuels by Tijero *et al.* [28], the available effective cross sections so far focus on a specific configuration of $(Th,Pu)O_2$. In case of Gd-doped LWR fuels (e.g., UO_2+Gd_2O_3), the calculation of the strongly neutron absorbing nuclides ^{155}Gd and ^{157}Gd becomes mandatory and can for instance be tackled by tabled effective cross sections that depend on both burn-up and initial radial position.

To generalise the previous developments, we propose a meta-model for the depletion calculation to be included in FPCs, enabling them to track the full evolution of minor actinides and the helium production rate. The main strength of the proposed meta-model is the standardized methodology which can be applied to different types of fuel materials (including MOX, which is the primary focus of the INSPYRE project) and different kind of reactors (with SFR and LFRs as first targets). The methodology is as follows (UO_2 in LWR is here used as an example of application, but the procedure can be easily generalized):

1. Run a set of SERPENT calculations[1] with different initial fuel compositions (e.g., enrichment e = 3%, 4%, 5%).
2. For each enrichment, collect (by detectors in the Monte Carlo calculation) the values of microscopic cross-sections at different burn-up values (e.g., bu = 0, 5, 10, 15, … GWd/t_{HM}).
3. Each microscopic cross-section is now available at discrete sampling points as a function of initial enrichment and local burn-up (e.g., the cross-section for reaction r of isotope X will be a discrete function as ${}^{X}\sigma_r(e, bu)$).
4. These discrete functions are expressed as two-entry tables and hardcoded as lookup tables in fuel performance codes.

[1] We consider an infinite lattice of fuel rods with typical volume ratios between fuel, cladding and coolant.

These steps are to be performed offline and only once. During the fuel performance simulation (online) the FPC simply performs an interpolation within the values in the table in terms of initial enrichment *e* and current local burn-up *bu*. This interpolation operation is essentially inexpensive. The last online operation required by the FPC is the solution of Bateman's equations, i.e., the depletion calculation itself. Since this last operation is decoupled from the generation of the microscopic cross-sections, it is essentially the solution of a system of linear ordinary differential equations (ODEs), namely

$$\frac{\mathrm{d}}{\mathrm{d}t}[\mathrm{X}]_i = \sum_{r,j} {}^{\mathrm{X}_j}\sigma_{r,j}(e,bu)\bar{\phi}[\mathrm{X}]_j - \sum_{r} {}^{\mathrm{X}_i}\sigma_{r,i}(e,bu)\bar{\phi}[\mathrm{X}]_i + \sum_{d,k} \lambda_{d,k}[\mathrm{X}]_k - \sum_{d} \lambda_{d,i}[\mathrm{X}]_i \qquad (3)$$

where $[\mathrm{X}]_i$ (at m^{-3}) is the concentration of isotope X_i, the first summation accounts for the reactions *r* on isotopes X_j resulting in X_i, the second summation accounts for the reactions *r* on isotope X_i, the third summation accounts for the decays *d* of isotopes X_k resulting in X_i, and the fourth summation accounts for the decays *d* of isotope X_i. $\bar{\phi}$ ($\mathrm{m}^{-2}\ \mathrm{s}^{-1}$) is the average local neutron flux, input of the depletion meta-model, ${}^{\mathrm{X}}\sigma_{r,i}(e, bu)$ (m^2) is the set of microscopic cross-sections function of burn-up *bu* and initial fuel enrichment *e*, and λ (s) are the decay constants. It is worth noting that the solution of Eqs. 3 does not require the application of predictor-corrector methods typical of depletion codes, since the cross-sections and the average local neutron flux do not explicitly depend on the isotope concentrations. This implies a further saving on the computational time when compared to full depletion approaches. It should be underlined that a direct coupling of the SERPENT and TRANSURANUS code has been developed for the simulation of Gd-doped UO_2 in the frame of the ESSANUF project, and that a similar coupling in the open source SALOME platform for nuclear reactor simulations is under development in the frame of the McSAFE project.

Currently we have applied this methodology to UO_2 in PWRs. We generated the lookup tables for microscopic absorption and fission cross-sections for relevant isotopes (up to ^{245}Cm). We implemented these tables in the SCIANTIX code. Moreover, we introduced in the code all the relevant decay constants, especially for the long-lived α-decay, which are key for the helium production rate. We implemented a first order implicit solver for the solution of the Bateman's equations given the macroscopic cross-sections and the decay constants.

The next steps in the development are going to be the verification of the meta-model for the UO_2/PWR case against SERPENT reference depletion calculations, the generation of microscopic cross-sections for the MOX/SFR and MOX/LFR cases (following the methodology 1 to 4), and lastly the verification of these cases. These future activities are to be performed within the SCIANTIX code prior to the inclusion of the meta-model in TRANSURANUS (objective of WP7.1 of INSPYRE).

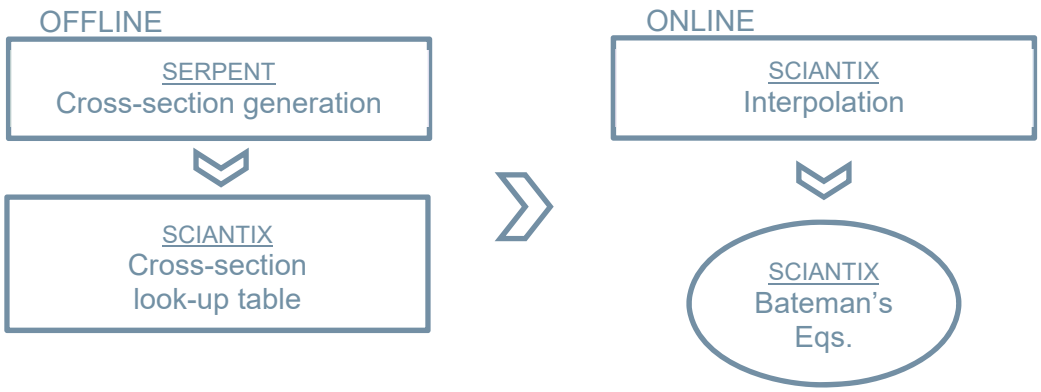

Figure 1: Sketch of the helium production meta-model, detailing the offline and online steps.

Diffusivity D_{He}. In the last fifty years several experiments[2] have been performed to investigate helium diffusivity in nuclear fuel [16], [29]–[39]. The experimental procedures available for measuring helium diffusivity differ mainly in the way in which the helium is introduced in the fuel samples. In particular, three introduction techniques are used: (i) infusion [29], [30], [32], [33], [40], [41], in which the sample is kept in a pressurized helium atmosphere for a certain infusion time, (ii) ionic implantation [34], [35], [37]–[39], in which a beam of $^3He^+$ hits and penetrates the sample, and (iii) doping [16], [36], in which α-decaying elements are introduced in the sample, resulting in an internal source of helium. These introduction techniques generate different helium distributions in the samples and induce different levels of damage to the crystal lattice of the sample [16], [42]. Depending on the introduction technique used, different measuring techniques are adopted to determine the concentration of helium introduced in the sample. A relation is then established between the helium concentration and the diffusivity [30], [32].

In the light of the profound differences in experimental techniques and in microstructure of the samples, the correlations derived from rough data fitting must be critically analysed. In fact, the spread of available diffusivities is extremely large. Nevertheless, currently used correlations for the helium diffusivity are still derived from rough data fitting [16], [35], [36], [39], [40] or are intended to be upper/lower boundaries enveloping the data [36], [43].

Following [44], the available experimental diffusivities are categorized depending on the technique used to introduce the helium in the samples (Table 1). With this categorization, two clusters of data become evident: the measurements performed via the infusion technique are in the lower region of the diffusivity range, whereas the measurements performed via the ion implantation and doping techniques lie in the upper region (Fig. 2). We ascribe this major clustering of the data to the different level of lattice damage induced by the different experimental techniques used to introduce helium in the samples. In particular, ion implantation and doping introduce additional defects in the crystal lattice of the sample [16], [22], enhancing diffusion. This conclusion is in line with the studies showing enhanced diffusion in hypo- and hyper-stoichiometric samples [22], [45], i.e., in samples characterized by somewhat altered crystal lattices. Considering the two data clusters, we propose two distinct empirical correlations for the helium diffusivity: one based on the data for infused samples and another one based on the data for implanted and doped samples. This implies that one correlation is suited for applications with no (or very limited) lattice damage, whereas the other is more suited for applications with significant lattice damage[3], which is consistent with the difference observed between the two sets of data obtained with the doping technique.
The proposed correlations are in the form $D = D_0 \exp(-Q/kT)$. Available data do not support the inclusion of other regressors besides temperature (e.g., only two data include plutonium concentration and each cluster includes only up to two microstructures). The best estimate correlation for the cluster of data with no or very limited lattice damage is:

[2] It is worth mentioning the important contribution to the studies on helium diffusivity arising from molecular dynamics (MD) calculations using empirical potentials [45], [80]. Yakub et al. [45] investigated both hypo- and hyper-stoichiometric UO_2. They concluded that small deviations from stoichiometry significantly accelerated helium diffusion, in agreement with the experimental results for hyper-stoichiometric samples [50]. Yakub suggests that non-stoichiometry increases helium diffusivity because it provides more paths for the movement of helium atoms within the lattice. This effect appears to be stronger in the hypo-stoichiometric domain [45], [81].

[3] The statement that each correlation herein derived should be applied in different situations depending on the lattice damage is meant as an indication, and not as a general conclusion. It is difficult to derive strong conclusions considering the limited numbers of available data. Nevertheless, this indication appears to be supported by the available data (within the temperature range covered by the available data).

$$D = 2.0 \cdot 10^{-10} \exp(-2.12/kT) \quad (4)$$

whereas for the cluster of data with significant lattice damage we get

$$D = 3.3 \cdot 10^{-10} \exp(-1.64/kT) \quad (5)$$

Every comparison between the two correlations, in terms of activation energy Q and pre-exponential factor D_0, represents an indication of a tendency. The available data are not enough to statistically support strong conclusions[4]. On the other hand, since we included all the available data in the fitting procedure, these correlations are the best available at this time. By fitting the two clusters of data (i.e., data from samples with no or very limited lattice damage and with significant lattice damage, respectively), we obtain an improved fitting quality. If data clustering is disregarded, the fit of all the data has a R^2 coefficient of determination of the linear regression of 0.43. Both these correlations are included in Fig. 2.

By propagating the uncertainties on the fitting parameters (see footnote 4) to the diffusivity, we estimate an uncertainty in the order of a factor of ten (x10) for the correlation relative to no or very limited lattice damage (Eq. 4) and a factor of one thousand (x1,000) for the correlation relative to significant lattice damage (Eq. 5). For comparison, the uncertainty of the fit made with the all data set is a factor of ten thousand (x10,000).

We recommend the correlation derived from data obtained using an ion implantation and doping technique in calculations for reactor and storage conditions. These experimental techniques introduce a certain level of lattice damage in the sample, which is similar to that suffered by the fuel in reactor and storage conditions. On the other hand, we recommend the use of the correlation derived from data obtained by infusion for calculations for fresh nuclear fuel. As for the selection of the diffusion coefficient to be used as D_{He} in Eqs. 1, 2, we should recommend using either Eq. 4 or Eq. 5, respectively if the model is used to simulate annealing or irradiation histories.

The model described in Eqs. 1, 2 is intended to represent the behaviour of helium *inside* fuel grains. Thus, from the perspective of this model[5], the diffusion coefficient should be referred to *single crystal* UO_2 (or either MOX). Nevertheless, the available data (Table 1) are not enough to support statistically the development of a correlation limited to single-crystal fuel.

The next step in the development is the inclusion of new experimental results in the data pool. These additional data (arising from experimental activities within the INSPYRE project) can either confirm the validity of the herein proposed correlations also for MOX fuel or allow for re-fitting of physically-grounded cluster of data indicating the difference within MOX and UO_2. Furthermore, for a more accurate description of helium diffusivity, information about the crystalline structure of the samples is envisaged. The exploration of other dependencies of the diffusivity is also useful for the derivation of accurate correlations, e.g., the stoichiometric deviation, the presence of crystal defects. Another fundamental step is the inclusion in the data pool of results arising from lower-length scale calculations.

[4] Summarizing the uncertainty analysis concerning the fit of the diffusivity correlations, it is important to notice that the functional form used is Log D = Log D_0 – Q/kT Log e. Thus, we have the following confidence intervals at 95% confidence level: Log D_0 (m^2 s^{-1}) = –9.7 (–11, –8.4) for Eq. 4, and –9.5 (–13, –5.8) for Eq. 5; Q (eV) = 2.12 (1.77, 2.56) for Eq. 4, and 1.64 (0.74, 2.56) for Eq. 5; the R^2 are respectively 0.93 and 0.52, for Eq. 4 and Eq. 5.

[5] It is worth remarking that the selection of the proper coefficient is model dependent. As an example, we could think of a model describing the absorption/desorption of helium from the gap in/from the fuel pellet. For such model, describing helium behavior at the scale of the pellet, the proper diffusion coefficient to be adopted should be referred to polycrystalline samples, since the pellet is a polycrystalline material.

Table 1: Collection of the helium diffusivities in UO_2 and $(U,Pu)O_2$.

Reference	Sample	Diffusivity ($m^2\ s^{-1}$)	Temperature (K)
Infusion			
Belle (1961)	UO_2 powder (≈0.16 µm)	$9.05 \cdot 10^{-22}$ $1.01 \cdot 10^{-20}$ $4.08 \cdot 10^{-20}$ $1.86 \cdot 10^{-19}$	968 1070 1166 1268
Rufeh (1964) **Rufeh *et al.* (1965)**	UO_2 powder (4 µm)	$1.5 \cdot 10^{-17}$	1473
Sung (1967)	UO_2 single-crystal (1 µm)	$6.14 \cdot 10^{-18}$ $9.15 \cdot 10^{-18}$ $12.57 \cdot 10^{-18}$	1473 1623 1773
Nakajima *et al.* (2011)	UO_2 single-crystal (18 µm)	$9.50 \cdot 10^{-10} \exp[-2.05/kT]$ $4.88 \cdot 10^{-10} \exp[-1.93/kT]$	range 1170–2110 range 1390–2070
Ion implantation			
Trocellier *et al.* (2003)	UO_2 polycrystal	$(3.7 \pm 0.74) \cdot 10^{-18}$	1273
Guilbert *et al.* (2004)	UO_2 polycrystal (8 µm)	$6 \cdot 10^{-17}$	1373
Roudil *et al.* (2004)	UO_2 polycrystal (10 µm)	$8 \cdot 10^{-9} \exp[-(2 \pm 0.1)/kT]$ $4 \cdot 10^{-10} \exp[-(2 \pm 0.1)/kT]$	range 1123–1273 range 1123–1273
Martin *et al.* (2006)	UO_2 polycrystal (24 µm)	$2.25 \cdot 10^{-17}$ $7.6 \cdot 10^{-17}$	1073 1373
Pipon *et al.* (2009)	$(U_{0.75},{}^{239}Pu_{0.25})O_2$ polycrystal	$9.2 \cdot 10^{-18}$ $1.6 \cdot 10^{-16}$	1123 1273
Garcia *et al.* (2012)	UO_2 polycrystal	$5 \cdot 10^{-10} \exp[-(1.4 \pm 0.2)/kT]$	range 973-1373
Doping			
Ronchi and Hiernaut (2004)	$(U_{0.9},{}^{238}Pu_{0.1})O_2$ polycrystal	$(8 \pm 2) \cdot 10^{-7} \exp[-(2.00 \pm 0.02)/kT]$	N/A
Talip *et al.* (2014a)	$(U_{0.999},{}^{238}Pu_{0.001})O_2$ polycrystal (10 µm)	$10^{-7} \exp[-2.59/kT]$	range 1320-1800

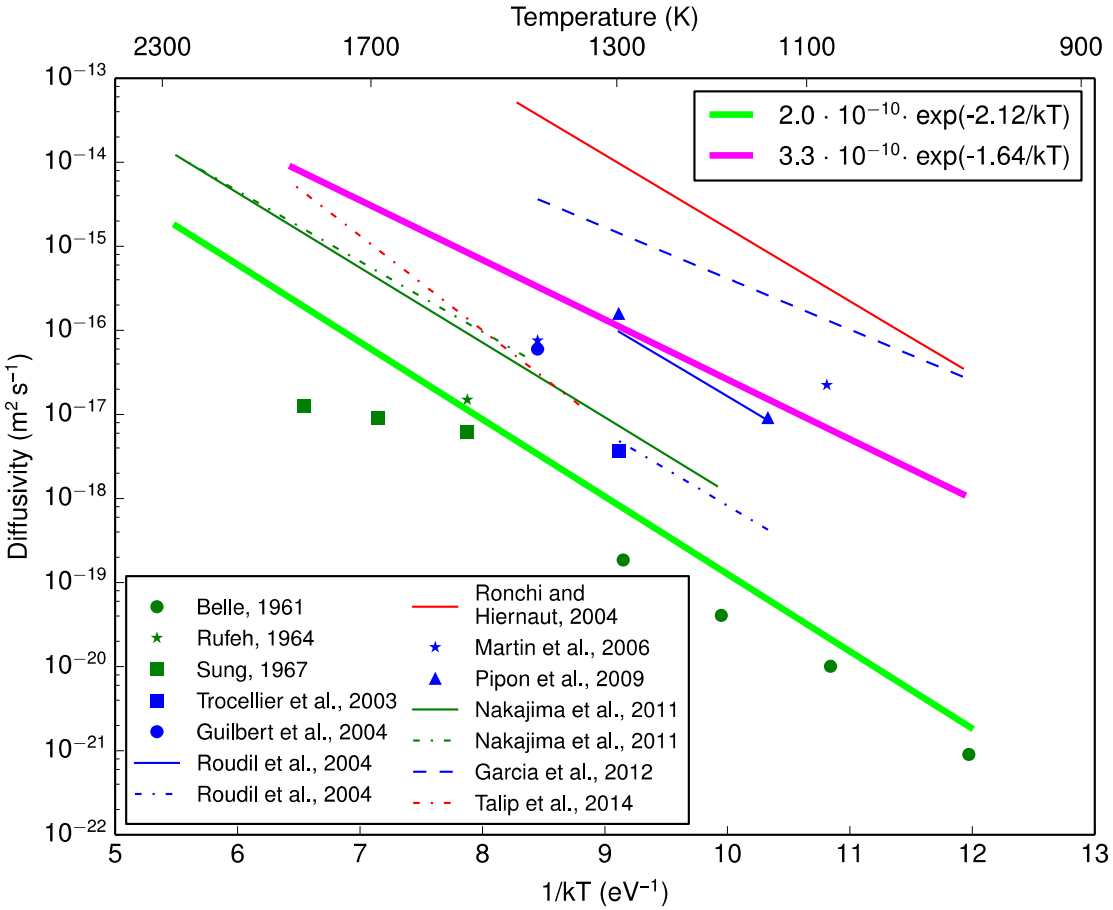

Figure 2: Plot of the experimental helium diffusivity in oxide fuel [44]. The measurements performed via the infusion technique (green) are clustered in the lower part of the plot, whereas in the upper part emerges a cluster of those measurements performed via the ion implantation (blue) and doping (red) technique. This clustering is ascribed to the different level of lattice damage caused to the sample by the different experimental techniques. Each cluster is fitted by a distinct correlation (magenta and light green).

Solubility $c_{S,\mathrm{He}}$. The goal is to establish a methodology for deriving solubility from available/new experimental data. To perform this, we derive new correlations for helium solubility based on an extensive overview of all the experimental results available in the open literature for UO_2. After the verification of the validity of Henry's law for the He-UO_2 system and the classification of the resulting data based on the sample microstructure, we derive empirical correlations for Henry's constant of helium in uranium dioxide. This methodology aims at the derivation of correlations after complete data analysis, data categorization and related uncertainty analysis.

As a starting point, we recall Henry's law $c_{S,\mathrm{He}} = k_H(T)p$ (6)

where k_H (at m^{-3} MPa^{-1}) is Henry's constant and p (MPa) is the helium pressure. The solubility is thus a function of temperature and pressure. If Henry's law is valid for the He-fuel system[6], Henry's constant is solely a temperature function.

[6] The validity of Henry's law in the system of interest can be verified with solubility data at different pressures and same temperature. The only dataset available with these characteristics is the one by [32], reported in Table 2. At each of three temperatures (1473 K, 1623 K, 1773 K) he performed infusions at three pressures

Following [46], we collect in Table 2 an overview of the available experimental data of solubility. Helium solubility in uranium dioxide have been also studied theoretically by [45], [47]–[49]. Olander [47] derived the helium solubility in UO_2 directly from atomic properties, basing the calculations upon a statistical-mechanical formula which assumes dissolved helium to behave as a simple harmonic oscillator in an interstitial site in the UO_2 lattice. Furthermore, Yakub *et al.*, [45], [50] performed molecular dynamics (MD) simulations determining the helium solubility in UO_2 as a function of temperature and UO_2 stoichiometry. Two-box MD simulations were performed in a wide range of helium pressures, from those achieved in infusion experiments (a few MPa) up to 4 GPa, as reported in [48]. The comparison of the simulation results for stoichiometric UO_2 with existing measurements shows a good agreement with the experimental data of helium solubility in single crystals. In addition, no essential deviations from the linear dependence of solubility on pressure was found up to around 0.5 GPa. Recently, Noirot [49] derived the theoretical value for Henry's constant applying to helium in interstitial positions in UO_2 a method devised to calculate the equilibrium concentration of point defects and gas atoms near a bubble in UO_2. First, the mechanical energy stored in the solid around an over-pressured bubble has been neglected, then considered. Noirot performed the calculations for different incorporation energies of a helium atom in an interstitial position and for different activation energies for the diffusion of helium in UO_2, obtaining consistent results both with the molecular dynamics computation and with the experimental data.

Assuming the validity of Eq. 6, to derive a solubility correlation to be used in Eqs. 1,2 we need to derive a correlation for Henry's constant as a function of temperature. The pressure value to be used for the trapping/re-solution processes is the partial pressure of helium in intra-granular bubbles, while for the boundary condition governing the diffusion towards the grain boundaries, the partial pressure of helium in inter-granular bubbles[7]. The data presented in Table 2 are reported in Fig. 3, divided based on the microstructure of the sample, i.e., powders and single crystals. As expectable, powders show a generally higher apparent Henry's constant in all the temperature range compared to single crystals, since helium is accumulated in-between different particles. Unfortunately, no data are available for polycrystalline materials (either experimental or lower-length scale simulation results).

Despite the large scatter of the experimental results for the helium solubility in uranium dioxide, the resulting clustering of the data motivated the derivation of two distinct correlations in the form $k_H = A\ \exp(-B/kT)$. The best estimate correlation for Henry's constant in the powder samples is

$$k_H = 1.8 \cdot 10^{25} \exp(-0.41/kT) \quad (7)$$

and the best estimate[8] correlation for Henry's constant in the single crystal samples is

$$k_H = 4.1 \cdot 10^{24} \exp(-0.65/kT) \quad (8)$$

(4.8 MPa, 6.9 MPa, 9.0 MPa) in a UO_2 single crystal of 1 μm size. The resulting solubilities show a reasonably linear dependency on pressure at each temperature, corroborating the verification of Henry's law. It is of sure interest to confirm the verification in this temperature-pressure range and to extend it outside of this range and to other fuel crystal sizes/fuel micro-structures. For this purpose, lower-length scale calculations and separate effects can be used in support one of the other.

[7] Very limited direct information about the pressure of either intra- and inter- granular bubbles is available at present. Further knowledge of these pressures, arising from separate effect experiments and lower-length scale calculations is of interest.

[8] Summarizing the uncertainty analysis concerning the fit of the solubility correlations, it is important to notice that the functional form used is Log k_H = Log A – B/kT Log e. Thus, we have the following confidence intervals at 95% confidence level: Log A (at m^{-3} MPa^{-1}) = 25.25 (23.91, 26.6) for Eq. 7, and 24.61 (23.41, 25.82) for Eq. 8; B (eV) = 0.41 (0.06, 0.75) for Eq. 7, and 0.65 (0.28, 1.01) for Eq. 8; the R^2 are respectively 0.83 and 0.83, for Eq. 7 and Eq. 8. These fitting parameters have been derived applying the LAR (least absolute residuals) method.

Regarding the applicability, the correlation derived fitting the data concerning the powder samples (Eq. 7) is usable for the analysis of the helium behaviour in the fuel after the pulverization occurred during LOCA-like temperature transients [51], [52]. On the other hand, the correlation proposed for Henry's constant in single crystals (Eq. 8) is of interest for calculations in mesoscale models dealing with single fuel grains (such as the herein proposed one, Eqs. 1,2).

The next step in the development is the inclusion of new results in the data pool. The consequence is going to be either the derivation of new dedicated correlations (if significant clustering arises) or the confirmation of the currently proposed ones. Data of relevance are of course those concerning the He-MOX system.

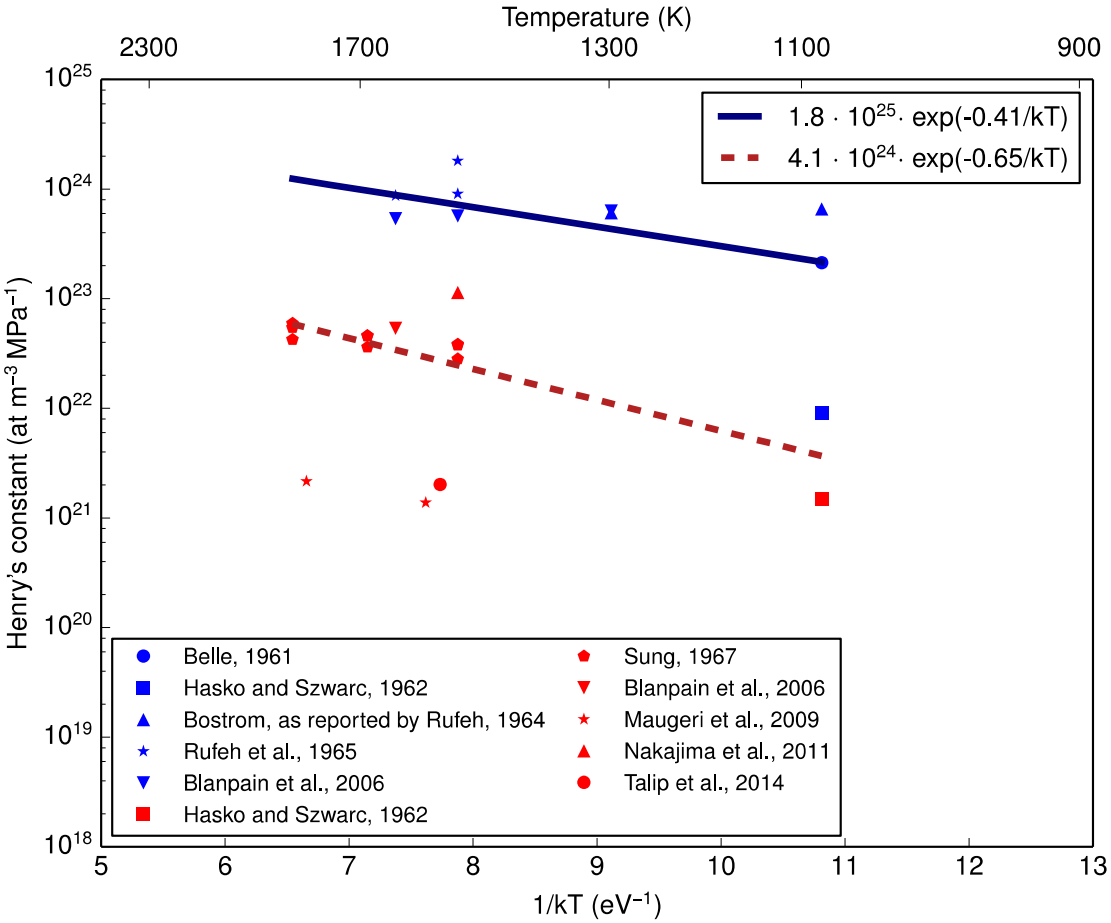

Figure 3: Plot of the experimental Henry's constant of helium in UO_2 classified depending on the microstructure of the sample (i.e., blue for the powder samples and red for the single crystal samples). Each cluster is fitted by a distinct correlation (bordeaux and blue navy) [46].

Table 2: Collection of the helium solubility in UO_2.

Reference	Sample	He infusion pressure (MPa)	Solubility (at m^{-3})	Temperature (K)
Powders				
Belle (1961)	UO_2 powder (≈0.16 µm)	0.1	$2.13 \cdot 10^{22}$	1073
Hasko and Szwarc (1963)	UO_2 powder	11	$9.91 \cdot 10^{22}$	1073
Bostrom (as reported by Rufeh, 1964)	UO_2 powder (≈0.15 µm)	0.1 0.1	$6.59 \cdot 10^{22}$ $3.08 \cdot 10^{22}$	1073 1273
Rufeh *et al.* (1965)	UO_2 powder (≈4 µm)	10 5 10	$1.81 \cdot 10^{25}$ $4.52 \cdot 10^{24}$ $8.72 \cdot 10^{24}$	1473 1473 1573
Blanpain *et al.* (2006)	UO_2 powder (≈10 µm)	0.2 0.2 0.2	$1.26 \cdot 10^{23}$ $1.14 \cdot 10^{23}$ $1.07 \cdot 10^{23}$	1273 1473 1573
Single crystals				
Hasko and Szwarc (1963)	UO_2 single crystal	11	$1.65 \cdot 10^{22}$	1073
Sung (1964)	UO_2 single crystal (≈1 µm)	4.8 6.9 9.0 4.8 6.9 9.0 4.8 6.9 9.0	$1.34 \cdot 10^{23}$ $2.61 \cdot 10^{23}$ $3.35 \cdot 10^{23}$ $1.72 \cdot 10^{23}$ $3.13 \cdot 10^{23}$ $4.05 \cdot 10^{23}$ $2.02 \cdot 10^{23}$ $4.05 \cdot 10^{23}$ $5.83 \cdot 10^{23}$	1473 1473 1473 1623 1623 1623 1773 1773 1773
Blanpain *et al.* (2006)	UO_2 single crystal (≈10 µm)	0.2	$1.07 \cdot 10^{22}$	1573
Maugeri *et al.* (2009)	UO_2 single crystal	100 100	$1.38 \cdot 10^{23}$ $2.16 \cdot 10^{23}$	1523 1743
Nakajima *et al.* (2011)	UO_2 single crystal (≈18 µm)	90	$1.03 \cdot 10^{25}$	1473
Talip *et al.* (2014)	UO_2 single crystal	98.7	$1.99 \cdot 10^{23}$	1500

2.2 Inert gas behaviour: columnar grains

The oxide fuel in fast reactors may undergo a restructuring process [5], [6]. Because of the high temperature and the extremely high temperature gradient, three microstructures originate within the fuel pellet. Radially, from the rim of the pellet towards its centre, three zones form: (1) an external (T < 1600°C) as-fabricated zone (unchanged density), (2) an intermediate (1600°C < T < 1800 °C) zone with equiaxed grains (higher density, grain-size of around 20 μm), and (3) an internal (T > 1800°C) zone with columnar grains (almost theoretical density, length of roughly 1 mm). The columnar grains are formed by the migration of the pores towards the centre by a mechanism of evaporation-condensation across the pore faces [6], [8], [53]. The pores gather in the centre of the pellet forming a central void.

For both as-fabricated and equiaxed grains, the description of inert gas behaviour is not substantially different from that of unrestructured oxide fuel, since the geometry of the grains is essentially unchanged [6], [20]. The classical description of IGB adopted in FPCs relies on [20], namely

$$\frac{\partial}{\partial \mathrm{t}} c_t = \mathrm{S} + \mathrm{D}_{\mathrm{eff}} \frac{1}{r^2} \frac{\partial}{\partial r} r^2 \frac{\partial}{\partial r} c_t \tag{9}$$

where c_t (at m^{-3}) is the total intra-granular gas concentration, S (at m^{-3} s^{-1}) is the production term, and $\mathrm{D}_{\mathrm{eff}}$ (m^2 s^{-1}) is the effective diffusion coefficient, a single parameter lumping the diffusion towards the grain boundaries, the trapping/re-solution rate of atoms in/from intra-granular bubbles. The diffusion operator is assumed to be the radial component of the Laplacian operator in spherical coordinates, since the grain shape is idealized as a sphere. The boundary condition is of Dirichlet type, assuming grain boundaries as perfect sinks.

The assumption of spherical grains, intrinsic in Eq. 9, is not suitable for the description of IGB in columnar grains since columnar grains are obviously of cylindrical shape. Moreover, the steep temperature gradient along the grain (around 200 °C/mm) causes a strong spatial variation of the diffusion coefficient. For these reasons, another approach is needed to include the description of IGB in columnar grains within the framework of FPCs.

The governing PDE of the diffusion in columnar grains is

$$\frac{\partial}{\partial \mathrm{t}} c_t = \mathrm{S} + \frac{1}{r} \frac{\partial}{\partial r} \mathrm{D}_{\mathrm{eff}}(T(r,t)) r \frac{\partial}{\partial r} c_t \tag{10}$$

where the effective diffusion coefficient is radially dependent[9]. For this reason, Eq. 10 is highly non-linear and its solution within FPCs is impractical. Eq. 10 should be solved at each time-step/iteration and in several mesh points of the thermo-mechanical simulation, in a multiscale fashion. The computational burden brought in by the multiscale solution of a non-linear PDE is clearly not in line with the computational requirement of FPCs.

We propose a reduced order model based on proper orthogonal decomposition and Galerkin projection (ROM-POD-G) [54]. The construction of the ROM is obtained in three steps

1. Collect a limited number of high-fidelity solutions[10], referred to as *snapshots*, of the governing PDE (Eq. 10). The snapshots are obtained through finite volume method (FVM).

[9] Again, the boundary condition is of Dirichlet type, assuming grain boundaries as perfect sinks.
[10] For the high-fidelity solution we used the in-house developed GrainThermoDiffusionFOAM solver, in the open source software OpenFOAM [82], solving the coupled energy and gas diffusion equations.

2. Calculate the basis where to project the governing equation, generating a reduced solution of the PDE. The POD approach handles this step in terms of an optimization problem, minimizing the L^2 error between the high-fidelity solution and the reduced one.
3. Apply the Galerkin projection on the governing PDE. Together with the approximation of the solution as a finite summation of time coefficients and basis, this step allows deriving an ODE linear system to be solved for the time coefficients.

These three steps are performed offline and then only the ROM is to be included in the online calculation of the FPC.

In the following, we showcase an example of application of the herein presented procedure. We show the construction of the ROM for the diffusion in a columnar grain, considering the temperature distribution due to the chosen power density and grain dimensions. As high-fidelity simulation, we assume a cylindrical grain of radius 10 μm and length 1 mm. The duration of the simulation is $6\ 10^6$ s (around 3 months, enough to reach the asymptotic solution for gas concentration[11]). The linear heat rate for the thermal problem is set to 40 kW m^{-1}, in the range targeted by FRs. The production rate of inert gas is set to 3.10^{18} at.m^3s^{-1}, coherently with the specific power corresponding to the linear heat rate, and the effective diffusion coefficient is $5\ 10^{-8}$ exp(−40'262/T) [55], [56].

Figure 4 reports the results of the high-fidelity simulation in terms of intra-granular inert gas concentration. It is useful to discuss the spatial distribution of the gas concentration within the grain. Along the grain axis, which is aligned with the pellet radius, there is a gradient of concentration opposed to the temperature gradient. This arises because of the temperature dependency of the diffusion coefficient. Higher diffusivity values towards the centre of the pellet compared to that towards the rim cause an accumulation of gas towards the rim (less diffusion to the grain boundaries, higher intra-granular concentration). This gradient along the grain axis causes a flux of gas along the axis, radially transferring gas from the outside to the inside of the grain. This behaviour implies a higher net release (more gas migrates in the higher temperature region) and is reproducible only with the solution of Eq. 10. As for the duration of the simulations, indicative of the computational effort of the high-fidelity model, it required around one hour on a i7 Intel 2.5 MHz with six parallel processes.

With the snapshots of the high-fidelity simulation, we generate the POD bases (Fig. 5). These bases are generated offline once and for all. They are parametric both in terms of the geometrical domain and in term of the operating conditions (linear heat rate, production rate of inert gas).

Figure 6 reports the results of the ROM-POD-G simulation. The spatial features and the asymptotic value of the solution are satisfactorily represented. The duration of the simulation, indicative of the computational effort of the ROM-POD-G model, is greatly below one second on a i7 Intel 2.5 MHz with one single process (a reduction of more than a factor of 20'000 compared to the high-fidelity model). The error analysis performed in terms of relative error on the average gas concentration and the L^2 error are presented in Fig. 7 and in Fig. 8, respectively. Both the error metrics show a satisfactory agreement between the two results. Considering the saving of computational time and the good accuracy (both quantitative and qualitative, as shown in the contour plots), this analysis demonstrates the effectiveness of this approach to describe the IGB in columnar grains within fuel performance codes.

[11] It is clear that the calculation of the asymptotic value is easier than the solution of Eq. 10. It could be argued that time-dependent solution of Eq. 10 is not useful because of the high value of the diffusion coefficient, rapidly bringing the system at its asymptotic value. This decision clearly depends on the reactor/fuel/power considered, therefore in our analysis we preferred the more general time-dependent approach. The methodological derivation and application of the ROM holds also for the stationary case.

Next steps of the development of this reduced order model are going to be dedicated to the span of the parameter space, i.e. to perform additional high-fidelity simulation with different linear heat rates and geometrical dimensions, to build a matrix of values among which interpolate to derive the final model. Last goal is the implementation of the ROM-POD-G in SCIANTIX and in TRANSURANUS and its application to MOX fuel simulations in FR conditions. Moreover, this methodological approach of combining reduced order modelling for multiscale simulations within the framework of fuel performance codes can be applied to other phenomena besides the IGB in columnar grains.

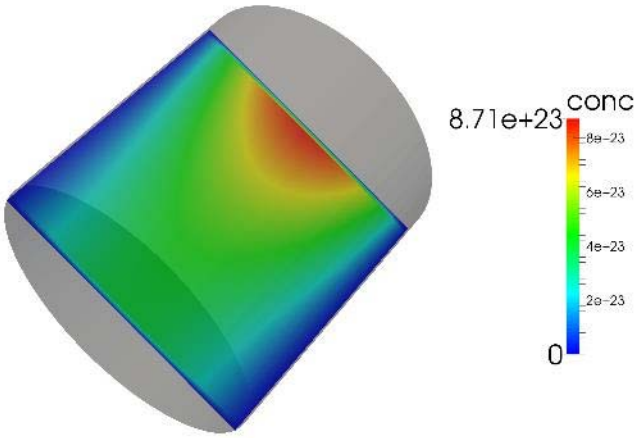

Concentration at 10^5 s

(a)

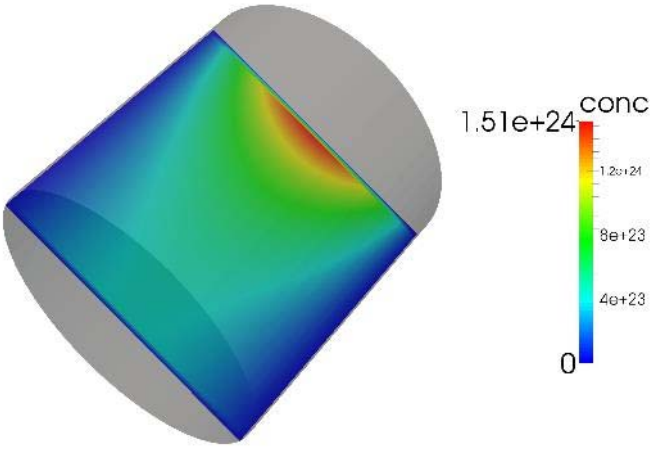

Concentration at 6 10^6 s

(b)

Figure 4. High-fidelity results of the OpenFOAM simulation of thermal diffusion and inert gas diffusion in a columnar fuel grain, at different times. The asymptotic value of the solution is reached in (b). The spatial dimensions of the grain are shown as normalized.

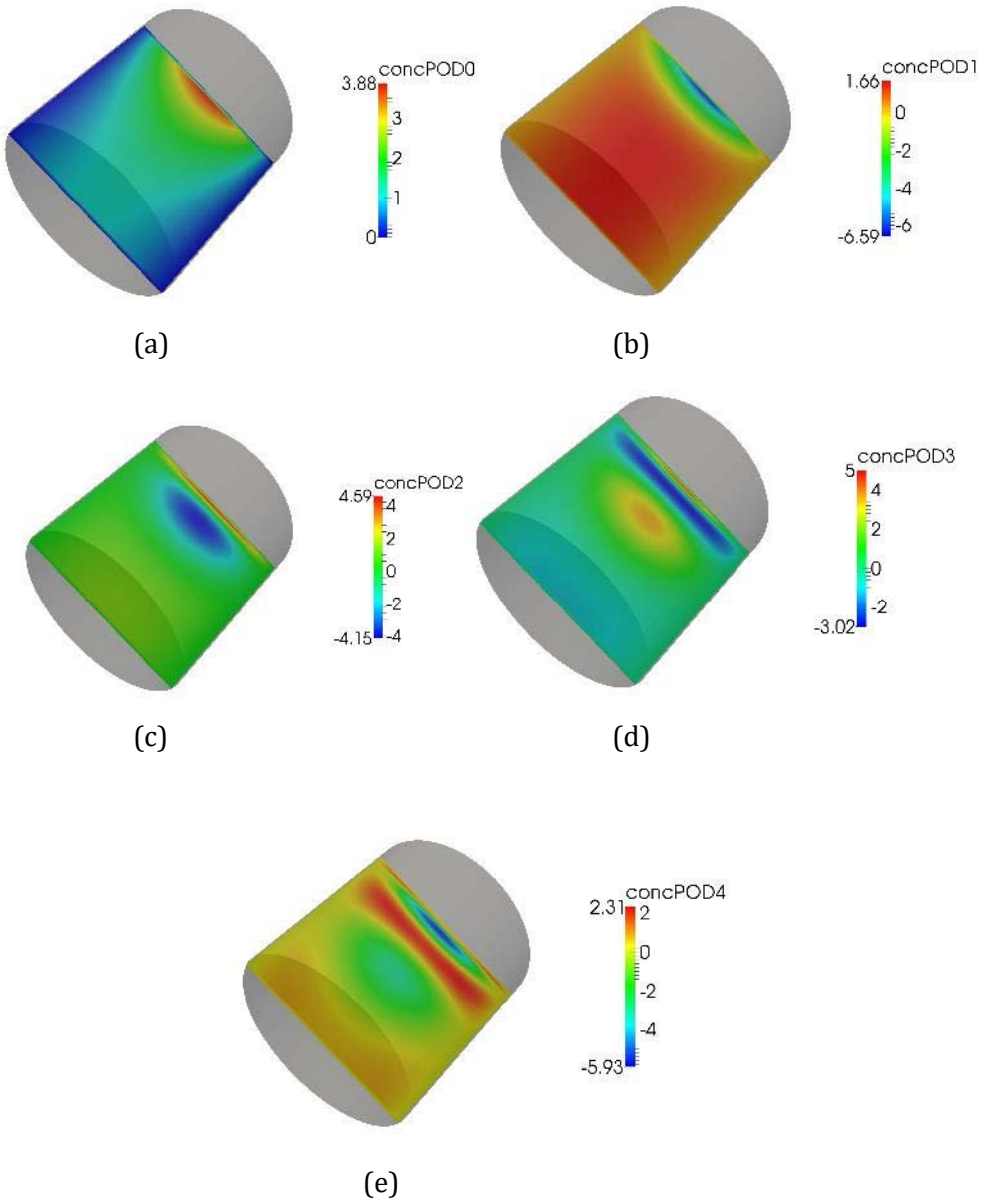

Figure 5. POD basis generated from the snapshots of the high-fidelity solution. These bases are parametrized in terms of the geometrical domain and the operating conditions.

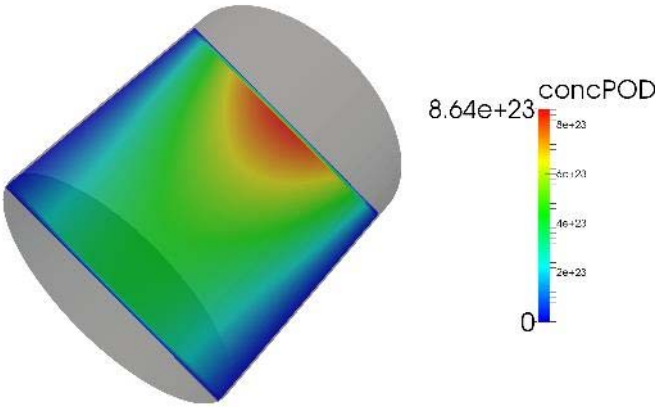

Concentration at 10^5 s

(a)

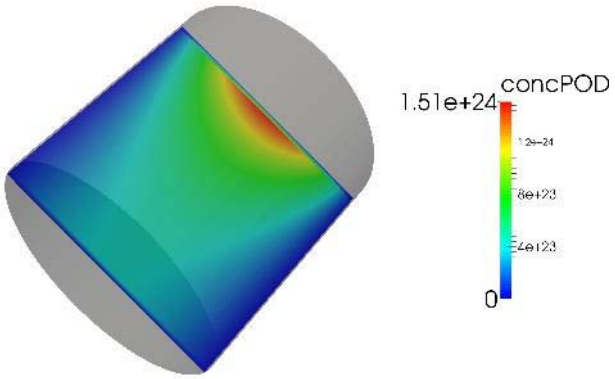

Concentration at 6 10^6 s

(b)

Figure 6. Reduced order model results of thermal diffusion and inert gas diffusion in a columnar fuel grain at various times. The asymptotic value of the solution is reached in (b). The spatial dimensions of the grain are shown as normalized. The comparison with Figure 4 is satisfactory.

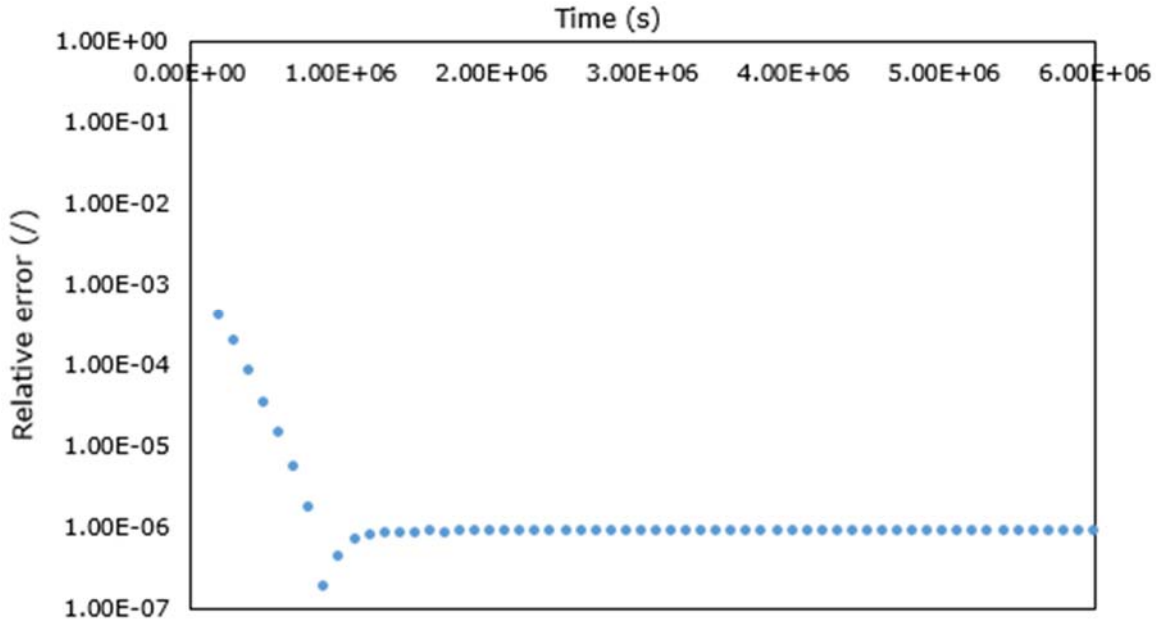

Figure 7. Relative error on the average gas concentration calculated by the ROM-POD-G with reference to the high-fidelity solution.

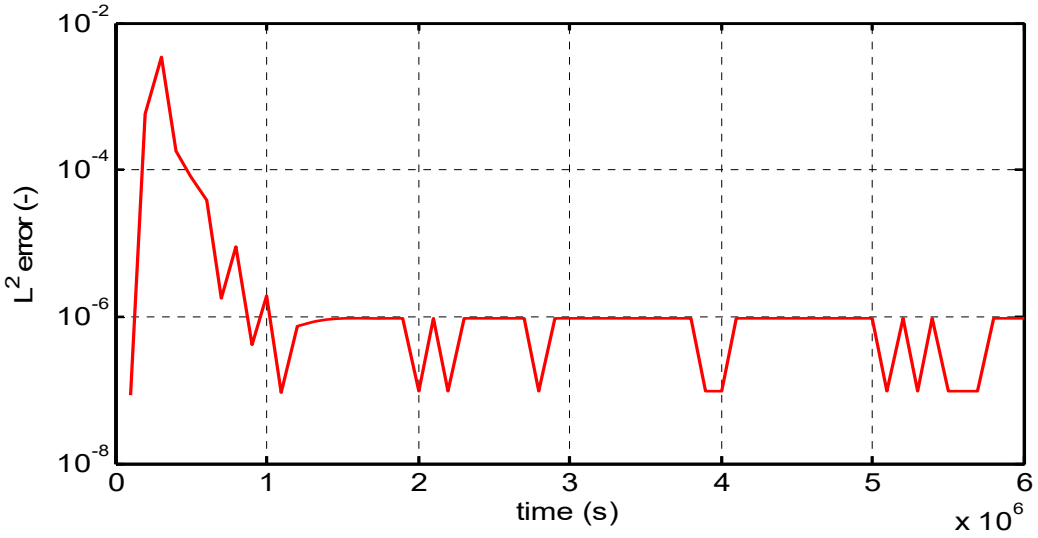

Figure 8. L^2 error on the gas concentration calculated by the ROM-POD-G with reference to the high-fidelity solution.

2.3 Inert gas behaviour: high burn-up structure

The combination of high local irradiation damage in nuclear oxide fuel, taking place, e.g., in the rim zone of the fuel pellets in light water reactors and in high-Pu content agglomerates in MIMAS mixed oxide, and low local temperatures promotes a dramatic restructuring of the as-fabricated microstructure, forming the so-called high burn-up structure (HBS). Although the physical processes occurring during the transition to the HBS have been deeply analysed and identified, their sequence is not fully understood.

HBS calls for a dedicated modelling approach. Its formation and its peculiar fission gas behaviour impact the local fuel thermal and mechanical properties, hence the overall performance of the fuel. Several semi-empirical and mechanistic models describing the evolution of the HBS has been developed and integrated in fuel performance codes [57]–[61]. On the other hand, HBS has been the object of intensive experimental campaigns in the last decades [52], [62]–[70]. Data are available on grain sizes at different degree of local restructuring [71]–[74], together with detailed characterization of restructured grains depletion of fission gas and local porosity evolution [52], [64].

Recently, Gerczak *et al.* [75] investigated the HBS formation in a standard PWR fuel rod through advanced electron microscopy techniques. In particular, their analysis was focused on the correlation between progressive polygonization and grain boundary surfaces orientations and showed how low-angle grain boundaries forms in place of the original high-angle grain boundaries of the as-fabricated microstructure. In the aforementioned work, the authors reported electron backscatter diffusion (EBSD) scans of a fuel pellet microstructure, taken at various distances from the pellet outer radius. Whilst reporting interesting images, the authors did not evaluate local burn-up, nor they provide information on the local fractional coverage of HBS with respect to the total area/volume.

As a starting point for the development of a new model suited in perspective for MOX fuel in FR conditions, we carried out new measurements on the average area covered by HBS at the different radial scans reported in the above-mentioned work. We employed these data to develop a new model describing HBS formation and grain depletion, extending an approach already proposed by Pizzocri *et al.* [57], [65]. In particular, this model extension is suited to naturally describe the formation and depletion of HBS in MOX fuels. Lastly, we present a preliminary assessment of the model against literature experimental data on grain depletion and discuss the potential application of the proposed model as a first step of an overall model for fission gas behaviour in UO_2 HBS.

First, in order to determine the radial burn-up profile in the considered sample, we simulated the mother fuel rod through TRANSURANUS, basing on the fuel rod characteristic and power history reported in [75], and reported in Table 3 and Fig. 9, respectively. In Figure 10, TRANSURANUS calculations of local burn-up and effective burn-up (i.e., the burn-up integrated below 1’000 °C, [76]) are reported.

The image analysis has been performed on the images taken from Figure 10 of [75] and reported here in Fig. 11 for the sake of completeness. TRANSURANUS predictions are fundamental to provide an estimation of the local burn-up to each radial location examined in the considered sample. In this work, we considered a subset of the reported images, focusing on the data obtained at relative radii equal to 0.63, 0.82, 0.94, and 0.95. We assume the image at 0.99 relative radius as representative for the complete restructuring process. This assumption is corroborated by the observed grain size, whose measurement yields approximately 200 nm, roughly corresponding to the observed, asymptotic grain size in the HBS [65], [77].

We measured the area covered by HBS in the analysed locations by the ImageJ software [78], and the results are collected in Table 4. Together with the measured area, we report an estimation of the volumetric fraction, which is calculated through the square-cube law.

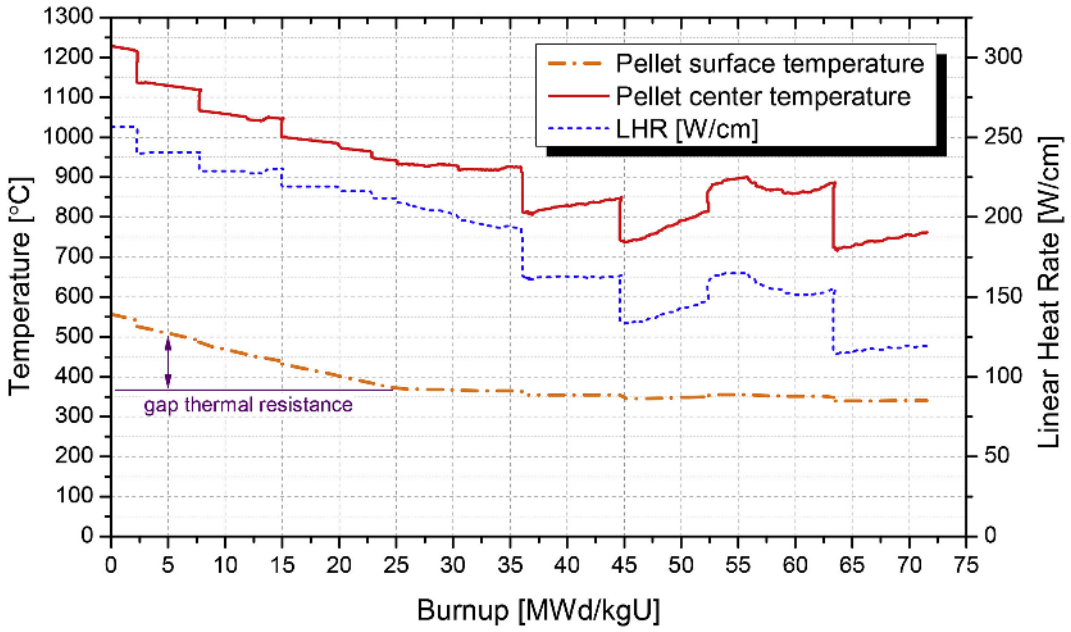

Figure 9. Linear heat rate and (estimated) pellet temperature profile as a function of burn-up for the considered specimen [75].

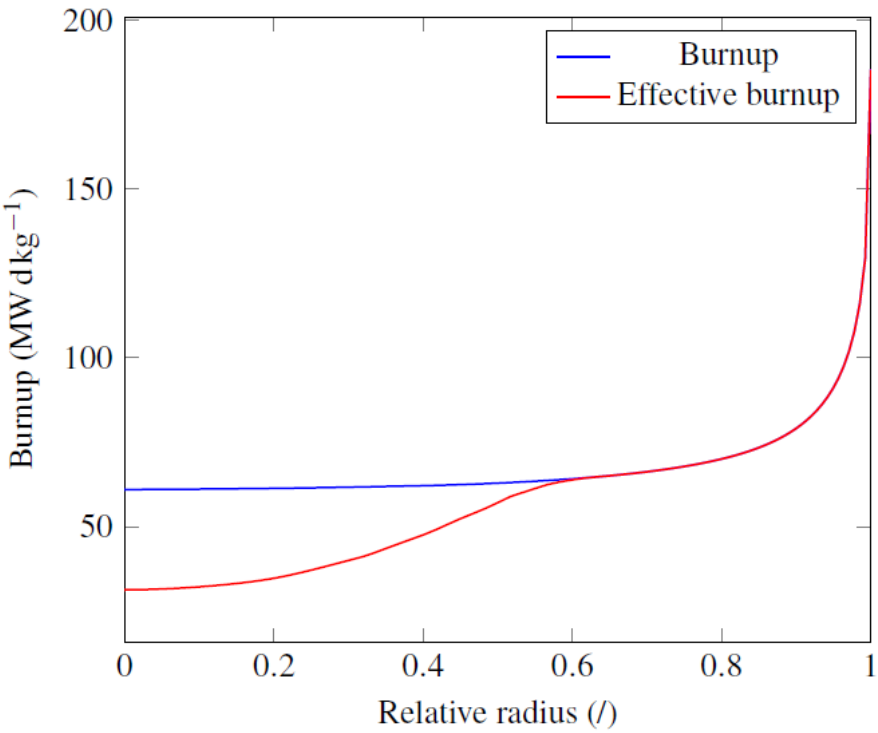

Figure 10. Calculated local burn-up and effective burn-up as a function of relative radius for the considered sample.

Table 3. Relevant characteristics of the considered fuel pin [75].

Characteristics	Value//Material
Cladding material	Zircaloy-4
Cladding outer diameter	10.77 mm
Cladding inner diameter	9.25 mm
Pellet-cladding gap	95 µm
Pellet diameter	9.06 mm
Pellet height	6.93 mm
Dish volume	1 %
^{235}U enrichment	2.9 %
Active fuel height	3660 mm
Fuel pin height	3860 mm
Specimen average burn-up	72 MWd kg_{HM}^{-1}
FGR	2.1 %

Table 4. Measured fraction of re-crystallized area in the selected locations.

Relative radius (/)	Effective burn-up (MWd t_{HM}^{-1})	HBS-covered area (/)	Estimated HBS-covered volume (/)
0.63	64.7	0.15	0.22
0.82	71.2	0.41	0.54
0.94	88.4	0.54	0.69
0.95	90.8	0.61	0.76

We employ the new experimental data to derive a correlation between the HBS-covered volume and the local effective burn-up. As a modelling choice, we correlate the complementary of the volumetric HBS coverage to the local burn-up, representative for the un-restructured portion of the material. Defining α (/) as the un-restructured volume over the total volume of the fuel, the data reported in Table 4 are fitted by a first-order differential model

$$\frac{\mathrm{d}}{\mathrm{d}bu_{\mathrm{eff}}}\alpha = -\frac{1}{\tau}\alpha \qquad (11)$$

considering the initial condition $\alpha(bu_{eff,0}) = 1$ and $bu_{eff,0} = 50$ MWd kg_{HM}^{-1}, i.e., no re-crystallization occurs until the chosen burn-up threshold is reached. The decay constant $\tau = 30$ MWd kg_{HM}^{-1} has been determined through a least-square fitting of the data reported in Table 4.

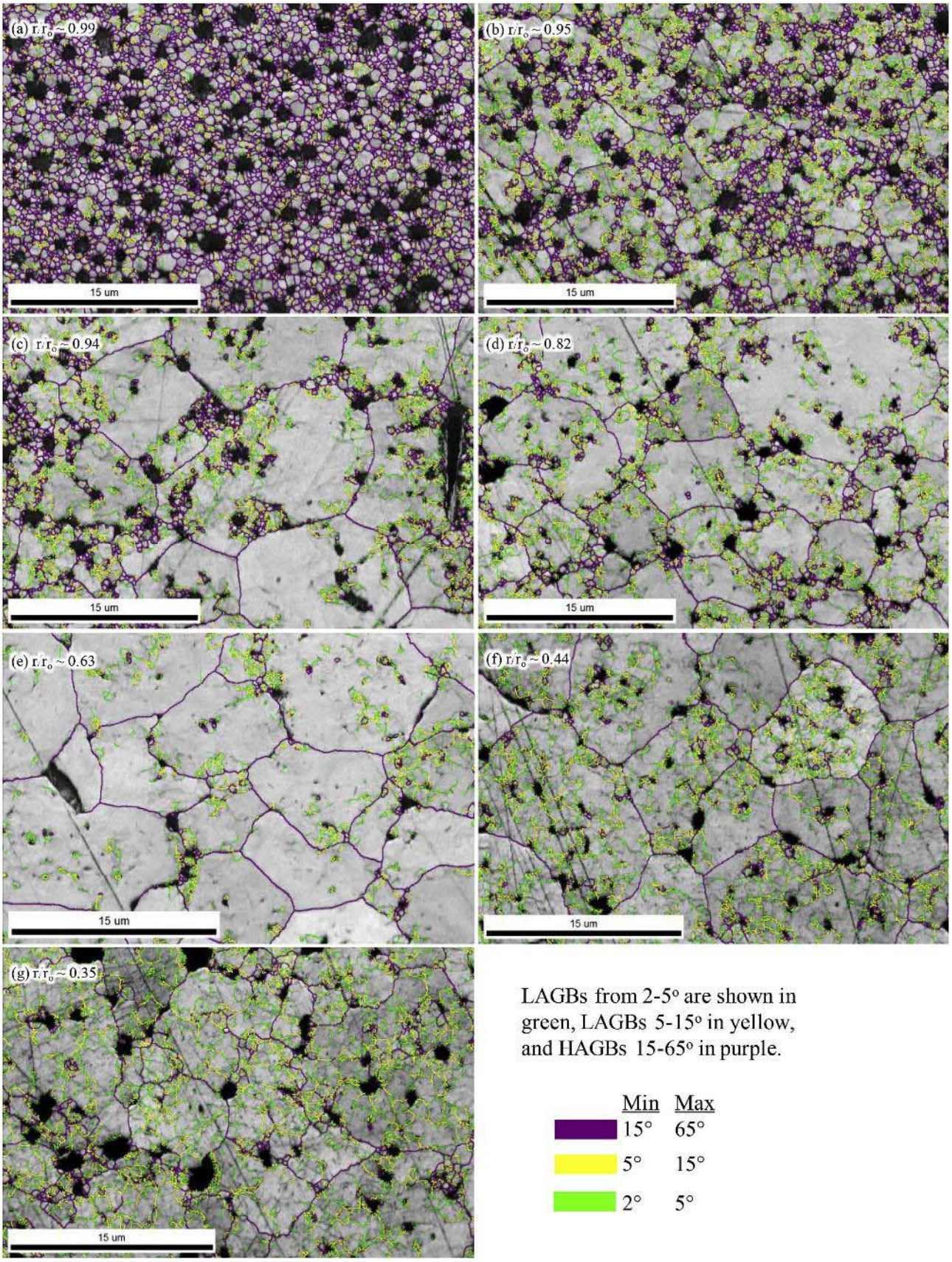

Figure 11. Grain boundary misorientation map overlaid on IQ map for locations r/r_0 0.99 to 0.35, through (g). taken from [75].

Differently from the model reported in Pizzocri *et al.* [57], this approach does not account directly for the observed effect of the initial grain size on the HBS formation, but this could be included in a better estimation of the threshold for HBS formation to occur, which in the present work is established as a constant value. Besides this, a larger initial grain size has an impact on the depletion of the grains, as will be described below. The solution of Eq. 11, together with the experimental data are reported in Fig. 12.

In the non-recrystallized region, intra-granular fission gas behaviour is described as proposed by Pizzocri *et al.* [14]. Fission gas atoms (Xe, Kr) are formed by the fissions in the matrix and can be trapped into small intra-granular bubbles or can diffuse towards grain boundaries, where a population of inter-granular bubbles arises. Moreover, fission fragments interact with existing intra-granular bubbles, causing the so-called re-solution of single gas atoms back into the fuel matrix. In engineering fuel performance codes, those processes are classically described by the following diffusion equation in spherical domain (identical to Eq. 9)

$$\frac{\partial}{\partial \mathrm{t}} c_t = \mathrm{S} + \mathrm{D_{eff}} \frac{1}{r^2} \frac{\partial}{\partial r} r^2 \frac{\partial}{\partial r} c_t \qquad (12)$$

where the gas production rate is assumed S (at m^{-3} s^{-1}) = 0.3 F, with 0.3 at $fiss^{-1}$ being the fission yield and F (fiss m^{-3} s^{-1}) is the fission rate. Eq. 12 is solved assuming a perfect sink grain boundary condition at the grain radius a (m) (i.e., $c_t(a,t) = 0$).

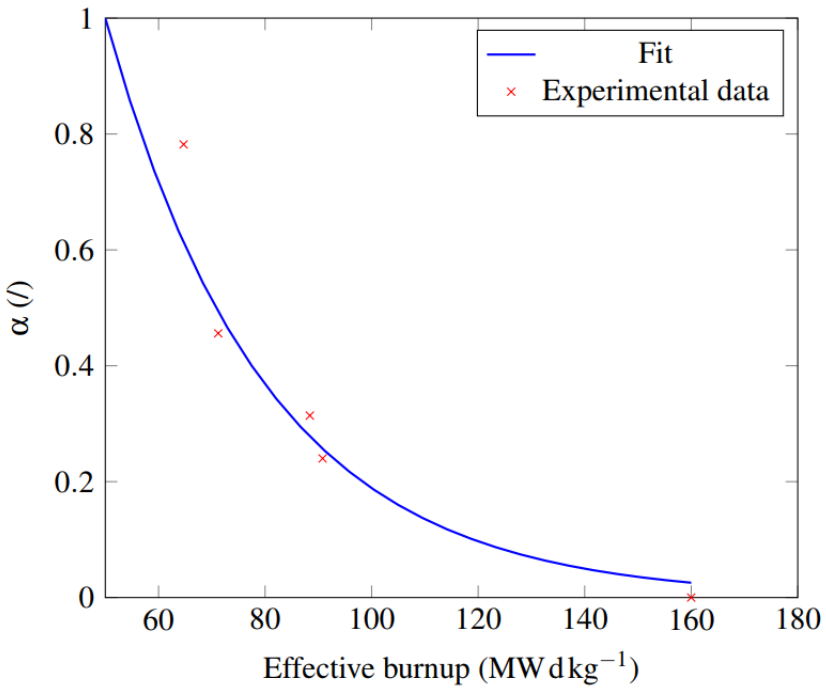

Figure 12. Experimental measurements of the non-recrystallized fuel volume and best fitting curve as a function of effective burn-up.

As HBS forms during irradiation, an increasing portion of the material is covered by the re-crystallized microstructure. When the effective burn-up threshold is reached, we consider a sweeping of gas concentration to the re-crystallized region equal to

$$\frac{\partial}{\partial bu_{\mathrm{eff}}} c_t^{\mathrm{HBS}} = -\frac{\partial}{\partial bu_{\mathrm{eff}}} c_t = -c_t \frac{\partial}{\partial bu_{\mathrm{eff}}} \alpha \qquad (13)$$

where c_t^{HBS} (at m^{-3}) is the total gas concentration in the HBS region. The total gas concentration in the HBS region is governed by a diffusion equation formally identical to Eq. 12, but considering a radius a_{HBS} = 150 nm, corresponding to the (constant) average values of the grain size when HBS formation is complete [57], [63], [73]. The total concentration of gas in the considered fuel volume, c_t*, is computed as

$$c_t^* = \alpha c_t \ + (1-\alpha) c_t^{HBS} \quad (14)$$

In Figure 13, we present a comparison of the predictions of the model presented above against experimental data by Walker [79], focusing on the intra-granular concentration of xenon. For the sake of comparison, we also report the results obtained according to the model proposed by Pizzocri *et al.* [57], considering the same initial radius (7.5 μm). The agreement with the experimental results is satisfactory, considering the highly heterogeneous experimental database, consisting in 35 samples having experienced different (and unknown) irradiation conditions. Moreover, we obtained these results using a fixed effective burn-up threshold for HBS to start forming at 50 MWd kg$_{HM}^{-1}$, based on previous works (e.g., [76], [79]). A deeper analysis of this threshold is of interest and is a perspective of this work. For the sake of completeness, we performed the simulation by the SCIANTIX code.

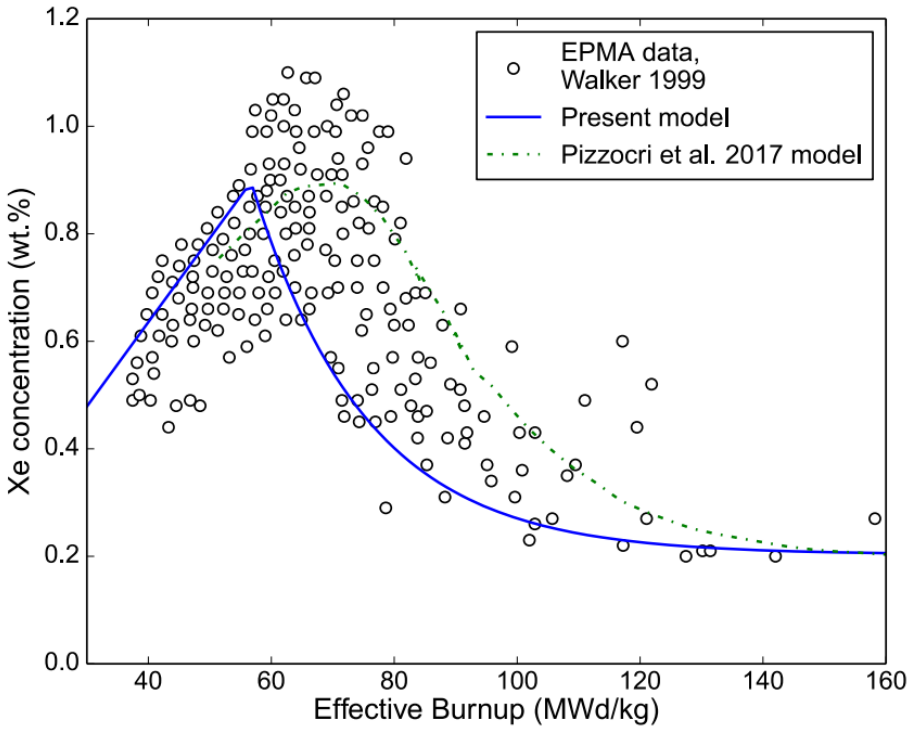

Figure 13. Comparison of intra-granular Xe concentration obtained by EPMA data by Walker [79] on different samples with the calculation of the present model. The results obtained with the model by Pizzocri *et al.* [57] are also reported. For the simulations, we used an initial grain size equal to 7.5 μm.

The next step in the development of this model will include data concerning MOX fuel in FR conditions. The HBS formation threshold is going to be revised, also accounting for lower scale information specific to MOX fuel, since currently available information are relative to UO_2. Moreover, the methodological approach proposed in this model can be extended for the description of plutonium islands in heterogeneous MOX fuels. In practice, dedicated IGB models for plutonium-rich particles, gray regions and depleted uranium grains can be developed and used consistently. This development is of interest beyond the specificity of HBS and can potentially represent a pivotal idea for modelling IGB in heterogeneous materials in a multiscale approach.

3 CONCLUSION AND FUTURE DEVELOPMENTS

In this deliverable, we described the status of the physics-based mesoscale models of fuel performance codes suitable to be further developed in the INSPYRE project. We focused on the development of an inert gas behaviour model suitable for simulation of MOX fuel in fast reactor conditions. It is worth clarifying that essentially no physics-based mesoscale models dedicated to MOX in FR conditions are currently available. For this reason, we selected models tailored for oxide fuels that have a potential for further development.

The first model presented is a physics-based description of helium behaviour. A complete review of available literature results has been carried out, with the objective of deriving physically grounded model parameters. The review herein presented covered all the data concerning helium-oxide fuels, for both helium diffusivity and helium solubility. New correlations for these critical parameters have been derived and are ready for use. Remarkably, these correlations can be used within the herein proposed physical-model or in other models available in fuel performance codes. Moreover, a meta-model for evaluating the helium production rate has been presented. This meta-model is based on look-up tables collecting average microscopic cross-sections generated offline with Monte Carlo neutronics calculations. With the considerable saving in computational effort brought about by look-up tables, this meta-model allows the calculation of the helium production rate in line with the requirements of a multiscale coupling with fuel performance codes. In addition, the meta-model calculates the complete burn-up depletion, providing valuable information besides the modelling of helium behaviour.

The second model concerns the treatment of gas diffusion in columnar grains. This problem is described by a non-linear partial differential equation, where the diffusion coefficient varies strongly along the grain axis due to the temperature distribution within the fuel pellet. To be able to solve this challenging problem with a computational effort in line with the requirements of fuel performance codes, we propose a reduced order model based on proper orthogonal decomposition and Galerkin projection. This reduced order model requires an offline phase to generate snapshots, i.e., several solutions of the high-fidelity model covering the parameter space of the problem. Once this offline step is performed, once, the reduced order model results in a limited system of linear ordinary differential equations able to accurately reproduce the high-fidelity solution to the problem. This approach is suitable for use in fuel performance codes and can be further extended to other phenomena that require a computationally intensive treatment.

The third model described concerns the formation of and the depletion of inert gas from the high burn-up structure. The herein proposed model extends models currently used for UO_2 in fuel performance codes. The extension is based on newly obtained measurements of the fraction of volume occupied by the HBS as a function of the effective burn-up, i.e., the burn-up integrated below a certain temperature threshold, used as a measure of the lattice damage. This approach is more consistent with the physical process of HBS compared to other state-of-the-art models and succeeds in naturally describing the depletion of intra-granular fission gas from the HBS region. Moreover, the approach proposed by this model can be extended to describe in a natural way the behaviour of inert gas in any heterogeneous material, including MOX fuel.

Specific details concerning the envisaged development path for each of these models are described at the end of each section. This development (including implementation in SCIANTIX, and where possible validation against separate effect experiments) will be performed in Task 6.1 prior to the implementation in codes in Task 7.1. We point out the fundamental role of new experimental data and lower scale calculation results coming from other WPs in INSPYRE to inform the models qualitatively (i.e., assumptions) and quantitatively (parameters), and to assess the mesoscale models herein presented.

4 REFERENCES

[1] S. B. Fisher *et al.*, "Microstructure of irradiated SBR MOX fuel and its relationship to fission gas release," *J. Nucl. Mater.*, vol. 306, no. 2–3, pp. 153–172, 2002.

[2] Y. H. Koo, B. H. Lee, J. S. Cheon, and D. S. Sohn, "Modeling and parametric studies of the effect of inhomogeneity on fission gas release in LWR MOX fuel," *Ann. Nucl. Energy*, vol. 29, no. 3, pp. 271–286, 2002.

[3] R. Parrish and A. Aitkaliyeva, "A review of microstructural features in fast reactor mixed oxide fuels," *J. Nucl. Mater.*, 2018.

[4] S. Yatabe, M. Floyd, and F. Dimayuga, "Canadian experience in irradiation and testing of MOX fuel," *J. Nucl. Mater.*, vol. 502, pp. 177–190, 2018.

[5] A. E. Waltar, D. R. Todd, and P. V. Tsvetkov, *Fast Spectrum Reactors*. 2012.

[6] D. R. Olander, *Fundamental Aspects of Nuclear Reactor Fuel Elements*. 1976.

[7] V. Di Marcello, A. Schubert, J. Van De Laar, and P. Van Uffelen, "Extension of the TRANSURANUS plutonium redistribution model for fast reactor performance analysis," *Nucl. Eng. Des.*, vol. 248, pp. 149–155, 2012.

[8] V. Di Marcello, V. Rondinella, A. Schubert, J. Van De Laar, and P. Van Uffelen, "Modelling actinide redistribution in mixed oxide fuel for sodium fast reactors," *Prog. Nucl. Energy*, vol. 72, pp. 83–90, 2014.

[9] Gen-IV, "Gen-IV," *https://www.gen-4.org/gif/jcms/c_59461/generation-iv-systems*, 2018. .

[10] ALFRED, "ALFRED," *http://www.alfred-reactor.eu/*, 2018. .

[11] MYRRHA, "MYRRHA," *https://sckcen.be/en/Technology_future/MYRRHA*, 2018. .

[12] L. Luzzi, A. Cammi, V. Di Marcello, S. Lorenzi, D. Pizzocri, and P. Van Uffelen, "Application of the TRANSURANUS code for the fuel pin design process of the ALFRED reactor," *Nucl. Eng. Des.*, vol. 277, pp. 173–187, 2014.

[13] G. Pastore, L. Luzzi, V. Di Marcello, and P. Van Uffelen, "Physics-based modelling of fission gas swelling and release in UO_2 applied to integral fuel rod analysis," *Nucl. Eng. Des.*, vol. 256, pp. 75–86, 2013.

[14] D. Pizzocri *et al.*, "A model describing intra-granular fission gas behaviour in oxide fuel for advanced engineering tools," *J. Nucl. Mater.*, vol. 502, pp. 323–330, 2018.

[15] K. Lassmann, A. Schubert, P. Van Uffelen, C. Gyori, and J. van de Laar, *TRANSURANUS Handbook, Copyright © 1975-2014*. Karlsruhe, Germany: Institute for Transuranium Elements, 2014.

[16] Z. Talip *et al.*, "Thermal diffusion of helium in ^{238}Pu-doped UO_2," *J. Nucl. Mater.*, vol. 445, no. 1–3, pp. 117–127, 2014.

[17] F. S. Ham, "Theory of diffusion-limited precipitation," *J. Phys. Chem. Solids*, vol. 6, no. 4, pp. 335–351, 1958.

[18] P. Lösönen, "On the behaviour of intragranular fission gas in UO_2 fuel," *J. Nucl. Mater.*, vol. 280, no. 1, pp. 56–72, 2000.

[19] D. R. Olander and D. Wongsawaeng, "Re-solution of fission gas - A review: Part I. Intragranular bubbles," *J. Nucl. Mater.*, vol. 354, no. 1–3, pp. 94–109, 2006.

[20] A. H. Booth, "A method of calculating fission gas diffusion from UO_2 fuel and its application to the X-2-f loop test," *At. Energy Canada Ltd. Chalk River Proj. Res. Dev. Rep. AECL-496*, no. 496, pp. 1–23, 1957.

[21] D. Pizzocri, T. Barani, and L. Luzzi, "SCIANTIX," *https://gitlab.com/poliminrg/sciantix*, 2018.

[22] Z. Talip *et al.*, "Helium behaviour in stoichiometric and hyper-stoichiometric UO_2," *J. Eur. Ceram. Soc.*, vol. 34, no. 5, pp. 1265–1277, 2014.

[23] VTT, "SERPENT," *http://serpent.vtt.fi/mediawiki/index.php/Main_Page*, 2018. .

[24] K. Lassmann, C. O'Carroll, J. van de Laar, and C. T. Walker, "The radial distribution of plutonium in high burnup UO_2 fuels," *J. Nucl. Mater.*, vol. 208, no. 3, pp. 223–231, 1994.

[25] K. Lassmann, C. T. Walker, and J. van de Laar, "Extension of the TRANSURANUS burnup model to heavy water reactor conditions," *J. Nucl. Mater.*, vol. 255, no. 2–3, pp. 222–233, 1998.

[26] A. Schubert, P. Van Uffelen, J. van de Laar, C. T. Walker, and W. Haeck, "Extension of the TRANSURANUS burn-up model," *J. Nucl. Mater.*, vol. 376, no. 1, pp. 1–10, 2008.

[27] P. Botazzoli *et al.*, "Extension and validation of the TRANSURANUS burn-up model for helium production in high burn-up LWR fuels," *J. Nucl. Mater.*, vol. 419, no. 1–3, pp. 329–338, 2011.

[28] J. I. Tijero Cavia *et al.*, "The TRANSURANUS burn-up model for thorium fuels under LWR conditions," *Nucl. Eng. Des.*, vol. 326, pp. 311–319, 2018.

[29] J. Belle, "Uranium Dioxide: properties and nuclear applications," pp. 569–589, 1961.

[30] F. Rufeh, "Solubility of helium in uranium dioxide," *M. S. Thesis, University of. California*, 1964.

[31] F. Rufeh, D. R. Olander, and T. H. Pigford, "The solubility of helium in uranium dioxide," *Nucl. Sci. Eng.*, 1965.

[32] P. Sung, "Equilibrium solubility and diffusivity of helium in single-crystal uranium dioxide," *PhD Thesis, Univ. Washingt.*, 1967.

[33] P. Trocellier *et al.*, "Application of nuclear reaction geometry for ^{3}He depth profiling in nuclear ceramics," *Nucl. Instruments Methods Phys. Res. Sect. B Beam Interact. with Mater. Atoms*, vol. 206, pp. 1077–1082, 2003.

[34] S. Guilbert *et al.*, "He migration in implanted UO_2 sintered disks," *J. Nucl. Mater.*, vol. 327, pp. 88–96, 2004.

[35] D. Roudil, X. Deschanels, P. Trocellier, C. Jégou, S. Peuget, and J. M. Bart, "Helium thermal diffusion in a uranium dioxide matrix," *J. Nucl. Mater.*, vol. 325, no. 2–3, pp. 148–158, 2004.

[36] C. Ronchi and J. P. Hiernaut, "Helium diffusion in uranium and plutonium oxides," *J. Nucl. Mater.*, vol. 325, no. 1, pp. 1–12, 2004.

[37] G. Martin *et al.*, "A NRA study of temperature and heavy ion irradiation effects on helium migration in sintered uranium dioxide," *J. Nucl. Mater.*, vol. 357, no. 1–3, pp. 198–205, 2006.

[38] Y. Pipon, C. Raepsaet, D. Roudil, and H. Khodja, "The use of NRA to study thermal diffusion of helium in (U, Pu)O_2," *Nucl. Instruments Methods*, vol. 267, no. 12–13, pp. 2250–2254, 2009.

[39] P. Garcia *et al.*, "A study of helium mobility in polycrystalline uranium dioxide," *J. Nucl. Mater.*, vol. 430, no. 1–3, pp. 156–165, 2012.

[40] K. Nakajima, H. Serizawa, N. Shirasu, Y. Haga, and Y. Arai, "The solubility and diffusion coefficient of helium in uranium dioxide," *J. Nucl. Mater.*, vol. 419, no. 1–3, pp. 272–280, 2011.

[41] E. Maugeri *et al.*, "Helium solubility and behaviour in uranium dioxide," *J. Nucl. Mater.*, vol. 385, no. 2, pp. 461–466, 2009.

[42] H. Labrim *et al.*, "Thermal evolution of the vacancy defects distribution in 1 MeV helium

implanted sintered UO_2," *Nucl. Instruments Methods Phys. Res. Sect. B Beam Interact. with Mater. Atoms*, vol. 261, no. 1–2 SPEC. ISS., pp. 883–887, 2007.

[43] E. Federici, A. Courcelle, P. Blanpain, and H. Cognon, "Helium production and behavior in nuclear oxide fuels during irradiation in LWR," *Proc. Int. LWR Fuel Perform. Meet. San Fr. Calif.*, pp. 664–673, 2007.

[44] L. Luzzi *et al.*, "Helium diffusivity in oxide nuclear fuel: Critical data analysis and new correlations," *Nucl. Eng. Des.*, vol. 330, pp. 265–271, 2018.

[45] E. Yakub, C. Ronchi, and D. Staicu, "Diffusion of helium in non-stoichiometric uranium dioxide," *J. Nucl. Mater.*, vol. 400, no. 3, pp. 189–195, 2010.

[46] L. Cognini *et al.*, "Helium solubility in oxide nuclear fuel:Derivation of new correlations for Henry's constant," *Nucl. Eng. Des.*, vol. 340, no. April, pp. 240–244, 2018.

[47] D. R. Olander, "Theory of Helium Dissolution in Uranium Dioxide. II. Helium solubility," *J. Chem. Phys.*, vol. 43, no. 3, pp. 785–788, 1965.

[48] E. Yakub, "Helium solubility in uranium dioxide from molecular dynamics simulations," *J. Nucl. Mater.*, vol. 414, no. 2, pp. 83–87, 2011.

[49] L. Noirot, "A method to calculate equilibrium concentrations of gas and defects in the vicinity of an over-pressured bubble in UO_2," *J. Nucl. Mater.*, vol. 447, no. 1–3, pp. 166–178, 2014.

[50] E. Yakub, C. Ronchi, and D. Staicu, "Computer simulation of defects formation and equilibrium in non-stoichiometric uranium dioxide," *J. Nucl. Mater.*, vol. 389, no. 1, pp. 119–126, 2009.

[51] A. Bianco, C. Vitanza, M. Seidl, A. Wensauer, W. Faber, and R. Macián-Juan, "Experimental investigation on the causes for pellet fragmentation under LOCA conditions," *J. Nucl. Mater.*, vol. 465, pp. 260–267, 2015.

[52] F. Cappia *et al.*, "Critical assessment of the pore size distribution in the rim region of high burnup UO_2 fuels," *J. Nucl. Mater.*, vol. 480, pp. 138–149, Nov. 2016.

[53] S. Novascone, P. Medvedev, J. W. Peterson, Y. Zhang, and J. Hales, "Modeling porosity migration in LWR and fast reactor MOX fuel using the finite element method," *J. Nucl. Mater.*, vol. 508, pp. 226–236, 2018.

[54] J. S. Hesthaven, G. Rozza, and B. Stamm, *Certified Reduced Basis Methods for Parametrized Partial Differential Equations*. 2015.

[55] K. Lassmann and H. Benk, "Numerical algorithms for intragranular fission gas release," *J. Nucl. Mater.*, vol. 280, no. 2, pp. 127–135, 2000.

[56] H. Matzke, "Gas release mechanisms in UO_2 - A critical review," *Radiat. Eff.*, vol. 53, pp. 219–242, 1980.

[57] D. Pizzocri, F. Cappia, L. Luzzi, G. Pastore, V. V. Rondinella, and P. Van Uffelen, "A semi-empirical model for the formation and the depletion of the high burnup structure in UO_2 fuel," *J. Nucl. Mater.*, vol. 487, pp. 23–29, 2017.

[58] K. Lassmann, C. T. Walker, J. van de Laar, and F. Lindström, "Modelling the high burnup UO_2 structure in LWR fuel," *J. Nucl. Mater.*, vol. 226, pp. 1–8, 1995.

[59] M. S. Veshchunov and V. E. Shestak, "Model for evolution of crystal defects in UO_2 under irradiation up to high burn-ups," *J. Nucl. Mater.*, vol. 384, no. 1, pp. 12–18, 2009.

[60] A. Bouloré, L. Aufore, E. Federici, P. Blanpain, and R. Blachier, "Advanced characterization of MIMAS MOX fuel microstructure to quantify the HBS formation," *Nucl. Eng. Des.*, vol. 281, no. October 2014, pp. 79–87, 2015.

[61] G. Khvostov, V. Novikov, A. Medvedev, and S. Bogatyr, "Approaches to modeling of high burn-up structure and analysis of its effects on the behaviour of light water reactor fuels in the START-3 fuel performance code," in *WRFPM-2005, Kyoto, Japan*, 2005.

[62] J. Spino, J. Rest, W. Goll, and C. T. Walker, "Matrix swelling rate and cavity volume balance of UO_2 fuels at high burn-up," *J. Nucl. Mater.*, vol. 346, no. 2–3, pp. 131–144, 2005.

[63] J. Spino, K. Vennix, and M. Coquerelle, "Detailed characterisation of the rim microstructure in PWR fuels in the burn-up range 40-67 GWd/tM," *J. Nucl. Mater.*, vol. 231, no. 3, pp. 179–190, 1996.

[64] J. Spino, A. D. Stalios, H. Santa Cruz, and D. Baron, "Stereological evolution of the rim structure in PWR-fuels at prolonged irradiation: Dependencies with burn-up and temperature," *J. Nucl. Mater.*, vol. 354, no. 1–3, pp. 66–84, 2006.

[65] T. Wiss *et al.*, "Properties of the high burnup structure in nuclear light water reactor fuel," *Radiochim. Acta*, vol. 105, no. 11, 2017.

[66] Y. Guerin, J. Noirot, D. Lespiaux, G. Chaigne, and C. Blanpain, "Microstructure evolution and in-reactor behvior of MOX fuel," in *ANS Int. Topical Meeting on LWR fuel performance, Park City, USA*, 2000.

[67] J. Noirot, L. Desgranges, and J. Lamontagne, "Detailed characterisations of high burn-up structures in oxide fuels," *J. Nucl. Mater.*, vol. 372, no. 2–3, pp. 318–339, 2008.

[68] J. Noirot, J. Lamontagne, N. Nakae, T. Kitagawa, Y. Kosaka, and T. Tverberg, "Heterogeneous UO_2 fuel irradiated up to a high burn-up: Investigation of the HBS and of fission product releases," *J. Nucl. Mater.*, vol. 442, no. 1–3, pp. 309–319, 2013.

[69] D. Baron, M. Kinoshita, P. Thevenin, and R. Largenton, "Discussion about HBS transformation in high burn-up fuels," *Nucl. Eng. Technol.*, vol. 41, no. 2, pp. 199–214, 2009.

[70] C. T. Walker, T. Kameyama, S. Kitajima, and M. Kinoshita, "Concerning the microstructure changes that occur at the surface of UO_2 pellets on irradiation to high burnup," *J. Nucl. Mater.*, vol. 188, no. C, pp. 73–79, 1992.

[71] C. Mieszczynski, C. Degueldre, G. Kuri, J. Bertsch, and C. N. Borca, "Investigation of irradiated uranium-plutonium mixed oxide fuel by synchrotron based micro X-ray diffraction," *Prog. Nucl. Energy*, vol. 57, pp. 130–137, 2012.

[72] C. Mieszczynski *et al.*, "Irradiation effects and micro-structural changes in large grain uranium dioxide fuel investigated by micro-beam X-ray diffraction," *J. Nucl. Mater.*, vol. 444, no. 1–3, pp. 274–282, 2014.

[73] I. L. F. Ray and H. Matzke, "Observation of a high burnup rim-type structure in an advanced plutonium – uranium carbide fuel," *J. Nucl. Mater.*, pp. 242–243, 1997.

[74] T. Sonoda *et al.*, "Transmission electron microscopy observation on irradiation-induced microstructural evolution in high burn-up UO_2 disk fuel," *Nucl. Instruments Methods Phys. Res. Sect. B Beam Interact. with Mater. Atoms*, vol. 191, no. 1–4, pp. 622–628, 2002.

[75] T. J. Gerczak, C. M. Parish, P. D. Edmondson, C. A. Baldwin, and K. A. Terrani, "Restructuring in high burnup UO_2 studied using modern electron microscopy," *J. Nucl. Mater.*, vol. 509, pp. 245–259, 2018.

[76] L. Holt, A. Schubert, P. Van Uffelen, C. T. Walker, E. Fridman, and T. Sonoda, "Sensitivity study on Xe depletion in the high burn-up structure of UO_2," *J. Nucl. Mater.*, vol. 452, no. 1–3, pp. 166–172, 2014.

[77] V. V Rondinella and T. Wiss, "The high burn-up structure in nuclear fuel," *Mater. Today*, vol. 13, no. 12, pp. 24–32, 2010.

[78] ImageJ, "ImageJ," *https://imagej.nih.gov/ij/*, 2018.

[79] C. T. Walker, "Assessment of the radial extent and completion of recrystallisation in high burn-up UO_2 nuclear fuel by EPMA," *J. Nucl. Mater.*, vol. 275, no. 1, pp. 56–62, 1999.

[80] G. Martin, S. Maillard, L. Van Brutzel, P. Garcia, B. Dorado, and C. Valot, "A molecular dynamics study of radiation induced diffusion in uranium dioxide," *J. Nucl. Mater.*, vol. 385, no. 2, pp. 351–357, 2009.

[81] K. Govers, S. Lemehov, M. Hou, and M. Verwerft, "Molecular dynamics simulation of helium and oxygen diffusion in $UO_{2\pm x}$," *J. Nucl. Mater.*, vol. 395, no. 1–3, pp. 131–139, 2009.

[82] OpenFOAM, "OpenFOAM," *https://www.openfoam.com/*, 2018. .